Rôle of elastic inhomogeneity in the development of cuboidal microstructures in Ni-based superalloys

M Cottura, Y Le Bouar, B Appolaire, A Finel

Rôle of elastic inhomogeneity in the development of cuboidal microstructures in Ni-based superalloys

M. Cottura[a,b], Y. Le Bouar[a,*], B. Appolaire[a], A. Finel[a]

[a] *LEM, Onera/CNRS, 29 av. de la division Leclerc, 92322 Châtillon, France*
[b] *Present address: CEA, DEN, Serv. Rech. Met. Phys., F-91191 Gif-sur-Yvette, France*

Abstract

A phase field model accounting for inhomogeneous and anisotropic elasticity has been used to investigate the consequences of inhomogeneous elasticity on the formation and coarsening of cuboidal microstructures in Ni-based superalloys. For that purpose, 2D and 3D calculations have been carried out considering high volume fractions of γ' precipitates, and accounting for their ordered crystal structure. The analysis of a substantial number of cases with different contrasts of elastic constants highlights the primary role played by the inhomogeneity $\Delta C'$ of the shear modulus C' on the shapes and spatial arrangements of the precipitates. This can be attributed to the sensitivity of the mechanisms involved in coarsening to $\Delta C'$. Finally, scanning electron micrographs of the AM1 superalloy are statistically analyzed and discussed in light of the calculations.

Keywords: Phase transformation, elasticity, phase field model, superalloys, coarsening

1. Introduction

Ni-based superalloys are materials developed for high-temperature applications such as aeronautic and industrial gas turbines. In particular, they are used in the hottest components of aero-engines such as turbine blades and vanes. The extensive use of monocrystalline superalloys for the design of such components is motivated by their excellent fatigue and creep properties at high temperature (up to 1100°C) under aggressive environments. These properties are controlled by some specific microstructure obtained by heat treatment. The optimal microstructure is composed of a high volume fraction of strengthening γ' precipitates ($L1_2$) dispersed in a matrix of γ phase

*Corresponding author
Email address: Yann.Lebouar@onera.fr (Y. Le Bouar)

(fcc solid solution) [1], as shown in Figure 1. It is well established that the peculiarities of this microstructure are due to the anisotropy of the elastic constants. But it is only recently that their inhomogeneity has also been put forward to explain a number of features in different superalloys [2]. The general purpose of the present work is thus to address this issue with careful and extensive phase field calculations.

Indeed, the phase field approach is the best suited for carrying such a work. Using this approach, several works have shown that elastic anisotropy [3, 4, 5, 6, 7], chemical order of the γ' phase [8, 9], and plasticity play important roles in microstructure evolutions under stress [10, 11, 12, 13, 14]. Comparatively, the role of elastic inhomogeneity has been much overlooked, probably because of the small differences between the elastic constants of γ and γ' usually reported in the literature. However, it is worth mentioning that the elastic inhomogeneity has already been accounted for in a few studies [3, 15, 16, 17, 18] and that its role has been highlighted in 2D [19].

Materials with cubic symmetry display three independent elastic moduli. In [19], the authors have used the following set of moduli for each phase: the 2D bulk modulus $B_{2D} = C_{11} + C_{12}$, the anisotropy coefficient $A = 2\,C_{44}/(C_{11} - C_{12})$ and the shear modulus $G = 2\,C_{44}$. Considering the influence of one of these moduli, while keeping the other two constant, on the microstructure evolutions of coherent two-phase systems, they have shown that the most pronounced effects are obtained with inhomogeneities of both A and G. However, more recently [21], it has been proposed that the microstructure of superalloys containing a high volume fraction of γ' precipitates is mainly sensitive to the inhomogeneity of a single relevant modulus, $\Delta C'$ where $C' = (C_{11} - C_{22})/2$ is another shear modulus. The importance of $\Delta C'$ has also been pointed out in an extensive analysis of experimental γ/γ' microstructures in different binary alloys [2]. Actually, the results obtained in [19] can be explained using $\Delta C'$ only, and it will be demonstrated in the present work that $\Delta C'$ is indeed an essential ingredient to explain shapes and arrangements of precipitates in superalloys.

Besides elasticity, microstructure evolutions in superalloys with high γ' fractions are also very sensitive to the chemical order displayed by γ' [8, 9]. Indeed, due to the symmetry breaking associated with the $\gamma \rightarrow \gamma'$ phase transformation, the γ' structure features four ordered variants: this difference in translation order is of prime importance because it prevents two neighboring precipitates with *out-of-phase* orders to merge by forming antiphase boundaries (APB). In Ni-based superalloys, the energy of APBs is very high, making them unstable with respect to wetting by γ. Then, out-of-phase neighboring γ' domains tend to always be separated by a thin layer of γ

phase, such that the coarsening process is deeply influenced: it is possible to merge two neighboring γ' precipitates only if they feature *in-phase* order.

From the points raised above, it is clear that a detailed analysis of the microstructure evolution in Ni-based superalloys containing a high volume fraction of γ' precipitates requires a model where both elastic inhomogeneity and chemical order are taken into account. To the best of our knowledge, this has been done only once in 2D in [20], where the elastic inhomogeneity has been described following the convention of [19]. Although the authors have found that increasing ΔA gives irregular domains whereas ΔG does not change much the microstructure, they have overlooked several important factors such as the presence of variants or the numerical width of the diffuse interfaces which are known to promote spurious coagulations [21, 22, 23] and irregular shaped γ' domains [8, 21].

In the present paper, we aim at providing a clear picture of the rôle played by elastic inhomogeneity in the microstructure evolution of Ni-based superalloys, with 2D and 3D phase field calculations. In particular, we will address whether one or two independent elastic inhomogeneities impact microstructure evolution. Moreover, we will investigate how the elastic inhomogeneity and the ordered character of the precipitates control the coarsening mechanisms in these alloys.

The phase field model is explained in the following section. Then, the results of 2D and 3D simulations are presented and discussed in §3 and §4, respectively. In the last section, we present a statistical analysis of the precipitate shapes in the industrial AM1 superalloy and discuss the results in light of our calculations.

2. Phase Field Model

At equilibrium, Ni-based superalloys feature both the disordered γ and ordered γ' phases. Following [11, 13, 18], the superalloy is modeled as an effective binary alloy. In that case, in addition to the local concentration field c($\underline{\boldsymbol{r}}$,t), three non-conservative structural fields $\eta_{i=1,3}(\underline{\boldsymbol{r}}, t)$ are introduced to account for the degeneracy of the low temperature γ' phase. The four translational variants of γ' are described by the following long-range order parameters: $\{\eta_1, \eta_2, \eta_3\} = \eta_0\{1,1,1\}$, $\eta_0\{\bar{1},\bar{1},1\}$, $\eta_0\{\bar{1},1,\bar{1}\}$, $\eta_0\{1,\bar{1},\bar{1}\}$.

The main ingredient of phase field models is a mesoscopic free energy functional F decomposed into a chemical F_{ch} and an elastic F_{el} contribution:

$$F = F_{ch}(c, \{\eta_i\}) + F_{el}(c, \{\eta_i\}, \underset{\sim}{\varepsilon}^{el}) \tag{1}$$

where $\underset{\sim}{\varepsilon}^{el}$ is the elastic strain tensor. These two contributions are described in §2.2 and §2.3.

2.1. Kinetic equations

The concentration and order parameters evolution is governed by kinetic equations relating time derivatives to the corresponding driving forces, defined as the functional derivatives of F with respect to the fields. Assuming linear constitutive relationships, the Cahn-Hilliard equation is used for the conserved concentration field and the Allen-Cahn equation for the non-conserved order parameter ones:

$$\frac{\partial c}{\partial t}(\underline{\boldsymbol{r}}\,,t) \;=\; M\nabla^2\frac{\delta F}{\delta c(\underline{\boldsymbol{r}}\,,t)} \tag{2}$$

$$\frac{\partial \eta_i}{\partial t}(\underline{\boldsymbol{r}}\,,t) \;=\; -L\,\frac{\delta F}{\delta \eta_i(\underline{\boldsymbol{r}}\,,t)} \tag{3}$$

The kinetic coefficients M and L, related to diffusion and structural relaxation respectively, are assumed constant. Following [11], M is such as to recover the interdiffusion coefficient in γ: $D \;=\; D_0\ exp(-\Delta U/k_BT)$ with $D_0 \;=\; 1.45\ 10^{-4}$ m^{2}s^{-1} and $\Delta U \;=\; 2.8$ eV [24]. We have used $L \;= 100\ M\ d^{-2}$, where d is the grid spacing, to ensure that kinetics is much faster for the order parameter than for the concentration field.

2.2. Ginzburg-Landau free energy

The chemical free energy accounts for the volume free energy associated with phase transformation and interface energies. This free energy is given by a standard Ginzburg-Landau functional:

$$F_{ch}(c,\{\eta_i\}) \;=\; \int_V f_{hom}(c,\{\eta_i\}) + \frac{\lambda}{2}\,|\nabla c|^2 + \frac{\beta}{2}\,\sum_i |\nabla\eta_i|^2 \;\; dV \tag{4}$$

where V is the volume, λ and β are gradient energy coefficients and $f_{hom}(c,\{\eta_i\})$ is the free energy density of a homogeneous system characterized by the concentration c and order parameters η_i.

The coefficients of the gradient term are related to the value of the interface energies and control the ratio between the γ/γ' interface and APB energies. They have been chosen isotropic as suggested by the spherical shapes of small precipitates in AM1 superalloys. As usual, $f_{hom}(c,\{\eta_i\})$ is approximated by a Landau polynomial expansion with respect to the order parameters. Its form

is dictated by the symmetry loss during the $\gamma \rightarrow \gamma'$ phase transformation. Following [18], the lowest possible order of the expansion, as well as a quadratic dependence on $c(\underline{\boldsymbol{r}})$, have been chosen:

$$f_{hom}(c,\{\eta_i\}) = \Delta f \left[\frac{1}{2}(c-c_\gamma^0)^2 + \frac{\mathcal{B}}{6}(c_2-c)\sum_{i=1,3}\eta_i^2 - \frac{\mathcal{C}}{3}\eta_1\eta_2\eta_3 + \frac{\mathcal{D}}{12}\sum_{i=1,3}\eta_i^4 \right] \tag{5}$$

where Δf is an energy density scale and c_2 an arbitrary concentration chosen between the equilibrium concentrations c_γ^0 and $c_{\gamma'}^0$ of the coexisting phases. $\mathcal{B}$, $\mathcal{C}$ and $\mathcal{D}$ are constants related to c_2, c_γ^0, $c_{\gamma'}^0$ and to the equilibrium long-range order parameter η_0.

In all the subsequent calculations, we have used the equilibrium concentrations $c_\gamma^0 = 0.15$ and $c_{\gamma'}^0 = 0.231$ (identified on the Ni-Al phase diagram at 950°C), as well as $c_2 = 0.18$. Following [18] with an equilibrium order parameter η_0 set to 1 gives $\mathcal{B} = 0.162$, $\mathcal{C} = 0.01458$ and $\mathcal{D} = 0.022842$. The non-dimensional gradient coefficients $\tilde{\lambda} = \lambda/(\Delta f d^2)$ and $\tilde{\beta} = \beta/(\Delta f d^2)$, where d is the grid spacing, are chosen as $\tilde{\lambda} = 0.21$ and $\tilde{\beta} = 9.75\ 10^{-4}$. This choice ensures that: (i) the interface width is large enough ($6d$) to avoid pinning on the numerical grid, (ii) antiphase boundaries in the γ' phase are wetted by the γ matrix, and (iii) the interface energy is equally generated by the gradient of the order parameter and concentration fields. Then, using 1D stress-free simulations, we compute the numerical interface energy $\tilde{\sigma} = 0.66\ 10^{-3}$ issued from the non-dimensional profile $(f_{hom}/\Delta f)$, $\tilde{\lambda}$ and $\tilde{\beta}$. $\tilde{\sigma}$ is related to the experimental interface energy through:

$$\sigma_{exp} = \tilde{\sigma}\, d\, \Delta f \tag{6}$$

For a given d, Δf can be deduced from (6). The γ/γ' interface energy σ_{exp} has a very low value in Ni-based superalloys [26, 7] and we have used throughout the paper 4 mJ.m^{-2}.

2.3. Elastic energy

In the framework of linear elasticity, the potential elastic energy reads:

$$F_{el}(\underline{\underline{\boldsymbol{\varepsilon}}}^{el}) = F_{el}^a(\underline{\underline{\bar{\boldsymbol{\varepsilon}}}}) + \frac{1}{2}\int_V \underline{\underline{\underline{\underline{\boldsymbol{\lambda}}}}} : \underline{\underline{\boldsymbol{\varepsilon}}}^{el} : \underline{\underline{\boldsymbol{\varepsilon}}}^{el}\ dV \tag{7}$$

where $\underline{\underline{\underline{\underline{\boldsymbol{\lambda}}}}}$ is the local elastic tensor and $\underline{\underline{\bar{\boldsymbol{\varepsilon}}}}$ is the average value of the total strain tensor $\underline{\underline{\boldsymbol{\varepsilon}}}(\underline{\boldsymbol{r}})$. $F_{el}^a(\underline{\underline{\bar{\boldsymbol{\varepsilon}}}})$ is a homogeneous term which depends on the choice of the driving conditions. In the present work,

where stress free conditions have been considered, $F_{el}^a = 0$. Assuming that the local concentration is the relevant field for discriminating the elastic properties, $\underset{\approx}{\boldsymbol{\lambda}}$ is assumed to depend linearly on c($\underline{\boldsymbol{r}}$) and is thus space dependent [18, 25]. In the small deformation framework, $\underset{\sim}{\boldsymbol{\varepsilon}}(\underline{\boldsymbol{r}})$ can be divided into two contributions:

$$\underset{\sim}{\boldsymbol{\varepsilon}}(\underline{\boldsymbol{r}}) \;=\; \underset{\sim}{\boldsymbol{\varepsilon}}^{el}(\underline{\boldsymbol{r}}) + \underset{\sim}{\boldsymbol{\varepsilon}}^{0}(\underline{\boldsymbol{r}}). \tag{8}$$

$\underset{\sim}{\boldsymbol{\varepsilon}}^{0}(\underline{\boldsymbol{r}})$ is the stress-free strain tensor associated with the lattice parameter change during the $\gamma \rightarrow \gamma'$ transformation. Assuming Vegard's law, it is given by:

$$\underset{\sim}{\boldsymbol{\varepsilon}}^{0}(\underline{\boldsymbol{r}}) \;=\; \varepsilon^T \, \Delta c(\underline{\boldsymbol{r}}) \, \underset{\sim}{\mathbf{1}} \tag{9}$$

where $\underset{\sim}{\mathbf{1}}$ is the identity matrix and $\varepsilon^T \;=\; \delta/(c^0_{\gamma'} - c^0_{\gamma})$. The misfit δ is related to the lattice parameters a_γ and $a_{\gamma'}$ of the stress-free γ and γ' phases $\delta \;=\; 2(a_{\gamma'} - a_\gamma)/(a_{\gamma'} + a_\gamma)$. The value $\delta = -0.1\%$ featured by AM1 superalloys at $T = 950°$C has been chosen [27, 28].

In the case of diffusion controlled phase transformations, static mechanical equilibrium can be assumed because the relaxation of the elastic waves is by orders of magnitude faster than the evolution of concentration and order parameters. Therefore, at each time step, elastic strain is computed by numerically solving mechanical equilibrium [18, 11].

3. 2D results

In this section, a systematic investigation on the influence of elastic inhomogeneity on the γ/γ' microstructures is performed in two dimensions. Then the key role of a particular shear modulus is demonstrated and explained using specific configurations.

3.1. Inhomogeneous elasticity

Because the elastic tensor of a cubic phase contains three independent coefficients, the elastic inhomogeneity of a coherent mixture of two cubic phases has to be defined on three quantities. Several sets of quantities may be selected such as the Voigt matrix coefficients C_{11}, C_{12}, C_{44}, the shear coefficient $C' = (C_{11} - C_{12})/2$, the Zener anisotropy ratio $A = C_{44}/C'$ or the bulk modulus $B = (C_{11} + 2C_{12})/3$. In this work, we have used the set (C', A, C_{11}) which was found particularly suited, as demonstrated below. Therefore, we introduce the three inhomogeneity parameters $\Delta M = (M_{\gamma'} - M_\gamma)/M_\gamma$ where $M = C'$, A or C_{11}.

The influence of the elastic inhomogeneity on the microstructure evolution is investigated by performing several calculations differing only by the value of the elastic constants. The elastic constants of γ are fixed and chosen representative of the γ phase in AM1. Then, the elastic constants of γ' are selected to provide the desired values of the three inhomogeneity parameters. The values used in the following simulations are listed in Tab. 1. As detailed below, we have generated several sets of elastic constants by relative variations of either $\pm 25\%$ or $+50\%$. Because the elastic constants $C_{11}^{\gamma'}$, $C_{12}^{\gamma'}$, $C_{44}^{\gamma'}$ are as usual defined with an accuracy of 1 GPa, the precise values of ΔC_{11}, ΔA and $\Delta C'$ slightly deviate from the targeted values (Tab. 1). Since the small deviations are not relevant in the present study, we have decided to clarify the reading of the text by referring to the set of parameters using the targeted values ($\pm 25\%/50\%$) rather than the actual ones.

The total size of the 2D simulations is 9.2×9.2 μm^2 discretized with 1024^2 nodes ($d = 9$ nm). All simulations are performed in stress-free conditions at $T = 950$°C during 4.8 h, and the initial configuration is always the same. This configuration (not shown) was previously generated using the AM1 elastic moduli (line *k* in Tab. 1) and a short annealing time (0.1 h) in order to get well-defined γ' precipitates with a mean size close to 300 nm.

First, two sets of elastic parameters ($C'_{\gamma'}$, $A^{\gamma'}$, $C_{11}^{\gamma'}$) corresponding to $\Delta C' = 0$ (a) and $\Delta C' = 50\%$ (f) have been selected with $\Delta C_{11} = 0$ and $\Delta A = 0$. Then, starting from these two cases, either a variation on ΔA of -/+ 25% (b/c - g/h) or on ΔC_{11}(d/e - i/j) has been applied. All values are given in Table 1. Using all the above sets of parameters, the microstructures obtained after 4.8 h of thermal annealing are presented in Figure 2.

It appears clearly that the microstructures in Figure 2 can be divided into two categories. The microstructures generated with $\Delta C' = 0$ exhibit precipitates of various sizes elongated along a cubic direction while with, $\Delta C' = 50\%$, the precipitates are mainly cuboidal with a narrower size distribution. This means that the value of ΔA (2.b-c or 2.g-h) and of ΔC_{11} (2.d-e or 2.i-j) have little impact on the γ/γ' microstructure whereas a variation of $\Delta C'$ induces strong changes (2.a-f).

To quantify the differences between the microstructures, each precipitate has been analyzed by binarizing $c(\vec{r})$ using the concentration in the middle of the interface as threshold value. Then, the aspect ratio of each precipitate can be determined as the ratio between the smallest and largest lengths of the precipitate along the cubic directions. These lengths were defined as quadratic standard deviations from the central position of the precipitate. Using these measurements, we have

characterized quantitatively the shape evolution of the precipitates by following the evolution of the average aspect ratio $\langle \ell_{min}/\ell_{max} \rangle$ during thermal annealing. In Figure 3, the empty squares ($\square$) and full circles ($\bullet$) correspond to measurements done in simulations with $\Delta C' = 0$ and $\Delta C' = 50\%$, respectively. Colors are used to distinguish the different simulations with labels referring to the elastic constants listed in Table 1.

First, these curves show that, after a short transient stage (0.5 h), the aspect ratio increases slightly when $\Delta C' = 50\%$ ($\bullet$) while it decreases significantly when $\Delta C' = 0$ ($\square$). After 4.5 h, all the simulations with $\Delta C' = 0$ predict an average aspect ratio of 0.68, significantly below 0.76, predicted when $\Delta C' = 50\%$. We also note that an increase/decrease of the inhomogeneity coefficients ΔA and ΔC_{11} do not affect significantly the aspect ratio. We can conclude from this quantitative analysis that the microstructure is almost only sensitive to the inhomogeneity on C'.

The above conclusion is consistent with the results of Hu et al. [19] who showed that strong microstructural changes occur when varying the Zener anisotropy while keeping C_{44} and B constant, or when varying C_{44} while keeping the the Zener anisotropy and B constant. However, our results are more accurate because they indicate that these strong changes originate from the variation of the inhomogeneity coefficient $\Delta C'$.

3.2. Inhomogeneity on C': $\Delta C'$

We have shown that for superalloys with high volume fractions of γ' featuring phases with a strong elastic anisotropy ($A \approx 3$), the microstructure is mainly sensitive to $\Delta C'$. In this section, we investigate in detail the consequences of this homogeneity in 2D.

A particular attention must be paid to the discretization length when studying microstructure evolutions in superalloys with high volume fractions of γ'. Indeed, in that case, the γ channels are very thin. Consequently, a channel width significantly larger than the interface width is required to avoid spurious coagulations between precipitates. When starting from a homogeneous supersaturated γ phase, this problem can not be fully avoided during the first stages of the microstructure evolution. However, once precipitates are well defined, the channels are sufficiently large with respect to the grid spacing and the spurious coagulations disappear progressively. In the present study, we have performed a detailed analysis of the influence of the grid spacing, and all the results presented below have been obtained using a grid spacing for which spurious coagulations are negligible during the coarsening stage.

Several calculations have been carried out in stress-free conditions using $\Delta C'$ values ranging from 0 to 50%. The real size of the system is 9.2×9.2 μm^2 discretized with 1536^2 nodes ($d = 6$ nm), and the initial condition is a homogeneous γ phase. The microstructure evolutions for $\Delta C' = 0$ and 50% are presented in Figure 4 where the grey corresponds to the γ matrix and the different colors are related to the four translational variants of the γ' phase.

The first stages of microstructure evolution are not sensitive to the value of $\Delta C'$. In both cases, after a thermal annealing of 0.06 h, the γ' domains have an average size of 80 nm and their volume fraction ($\tau_{\gamma'} = 0.65$) is already close to the late stage value ($\tau_{\gamma'} = 0.61$ at $t = 12$ h). The four variants of the $L1_2$ structure are randomly distributed with equal probabilities. The small precipitates are circular, as expected with an isotropic surface energy. The large precipitates already display anisotropic shapes resulting from the anisotropy of the elastic interactions. When $t = 0.6$ h, the average precipitate size has increased up to 106 nm due to coarsening. Most precipitates adopt a well defined cuboidal shape and tend to align along the cubic directions.

The consequences of $\Delta C'$ appear clearly on the subsequent microstructure evolution. With $\Delta C' = 0$, precipitates align along soft elastic directions to form sheets composed of several γ' domains. Inside these sheets, the γ' domains are only separated by thin matrix layers. The distance between parallel neighboring sheets is rather large and the microstructure contains many elongated precipitates. On the contrary, with $\Delta C' = 50\%$, the microstructure is mainly composed of cuboidal precipitates with aspect ratios close to 1. Alignments of precipitates along cubic directions are also clearly visible, but neighboring precipitates are always separated by significant layers of γ phase. No γ' sheets are observed. At the end of the simulation, the number of precipitates is slightly higher (127 instead of 85 when $\Delta C' = 0$) and the average precipitate volume is correlatively slightly smaller (0.042 μm^2 instead of 0.063 μm^2).

The sensitivity of the precipitate shape to the inhomogeneity coefficient $\Delta C'$ is quantitatively analyzed in Figure 5 where the time evolution of the average aspect ratio $\langle \ell_{min}/\ell_{max} \rangle$ is shown for different values of $\Delta C'$. When the annealing time is shorter than $t = 0.6$ h, no distinction can be made between the different average aspect ratios, which is consistent with the microstructure evolutions in Figure 4. Then, the average aspect ratio starts to be increasingly sensitive to the inhomogeneity on C'; the higher values of $\Delta C'$ lead to cuboidal precipitates whereas more elongated precipitates are obtained with lower values of $\Delta C'$. After 2 h, the aspect ratio increases continuously with $\Delta C'$. Although plateaus at long times ($t > 3.7$ h) are not well established because of the

fluctuations displayed by the curves, the final value of the aspect ratio is estimated by averaging over the last 40 minutes of annealing (3.7 h $< t <$ 4.5 h). As shown in Figure 5 (bottom), the average aspect ratio increases linearly from 0.67 at $\Delta C' = 0$ to 0.78 at $\Delta C' = 50\%$.

In conclusion, we have shown that the inhomogeneity coefficient $\Delta C'$ controls the shape of the precipitates in superalloys with high volume fractions of γ' and that the average aspect ratio is a relevant indicator to quantify the morphological changes.

3.3. Coarsening mechanisms

In this section, we analyze the mechanisms responsible for the coarsening of the γ/γ' microstructure, and we investigate how these mechanisms are sensitive to the value of the inhomogeneity $\Delta C'$.

Two mechanisms contribute to the coarsening of a microstructure containing high volume fractions of precipitates. The first one is the Ostwald ripening, where large precipitates grow at the expense of smaller ones by exchanging solute in the matrix by diffusion. The second one is the coagulation of neighboring precipitates. In addition, in the γ/γ' microstructures considered in this work, the ordered character of γ' strongly influences the coarsening process. Indeed, because the γ/γ' interface energy is smaller than half the antiphase boundary (APB) energy, APBs are never observed inside γ' precipitates and the coagulation of different translational variants is prevented. Finally, the coherency stresses generated by the misfit induce long range anisotropic interactions which may generate the attraction, repulsion or alignment of precipitates. This is expected to strongly impact the coarsening process and may even give rise to some local inverse coarsening [29].

We have analyzed the coarsening mechanisms after $t = 1$ h, i.e. when the γ' precipitates and γ channels are well defined and when the average aspect ratio is already sensitive to the elastic inhomogeneity (Fig. 6). Whatever the value of $\Delta C'$, the Ostwald ripening is always the main coarsening mechanism (Fig. 6 - black arrows), and the occurrence of coagulations of precipitates (Fig. 6 - red arrows) is strongly related to the value of $\Delta C'$. When $\Delta C' = 0$, 23% of the coarsening events are coagulations whereas they are less than 8% when $\Delta C' = 50\%$. To conclude, the final microstructure contains almost 1/4 of neighboring γ' precipitates which are in-phase when $\Delta C' = 50\%$.

To explain why $\Delta C'$ plays such an important role on the coarsening process, simple configurations are now considered. The elastic energy is written as the sum of 3 independent modes

associated with the bulk modulus B and the two shear elastic moduli C' and C_{44}:

$$\begin{aligned} F_{el} = \quad & \tfrac{B}{2}\ (Tr\,\underset{\sim}{\varepsilon}^{el})^2 + 2\,C_{44}\ \left[(\varepsilon_{12}^{el})^2 + (\varepsilon_{13}^{el})^2 + (\varepsilon_{23}^{el})^2\right] \\ + \quad & \tfrac{C'}{3}\left[(\varepsilon_{11}^{el} - \varepsilon_{22}^{el})^2 + (\varepsilon_{22}^{el} - \varepsilon_{33}^{el})^2 + (\varepsilon_{11}^{el} - \varepsilon_{33}^{el})^2\right] \end{aligned} \tag{10}$$

where B is given by $(C_{11} + 2\,C_{12})/3$ and $Tr\,\underset{\sim}{\varepsilon}^{el}$ is the trace of the elastic strain tensor.

First, the elastic strain fields corresponding to each mode are shown in Figure 7 for a single cuboidal precipitate. The elastic energy related to C' is mainly localized along the edges of the precipitate, while the energy densities located near the corners and inside the precipitate are linked to the C_{44} and B modes, respectively. This indicates that the coagulation of γ' precipitates resulting from the shrinkage of the matrix channels should be more sensitive to the value of the elastic moduli C' than to C_{44} or B.

Next, the elastic interaction between two aligned cuboidal precipitates of size ℓ_1 is considered. As in the previous calculations, the precipitate/matrix interface is smooth and contains 6 grid points, but we have checked that the results are not sensitive to the interface thickness. The elastic energy F_{el} is plotted in Figure 8 versus the width ℓ_2 of the channel separating the precipitates. In agreement with [30, 31, 32], the elastic energy is minimum for a distance ℓ_2^0 close to $\ell_1/2$. Therefore, particles separated by a distance larger (resp. smaller) than ℓ_2^0 attract (resp. repel) each other. In addition, Figure 8 shows that the equilibrium distance ℓ_2^0 increases by 20% as $\Delta C'$ increases from 0 to 50%.

When the volume fraction of precipitates is high as in the present work, the distance between precipitates is, in average, necessarily smaller than half the precipitate size. Indeed for $\tau_{\gamma'} \approx 0.61$, $\ell_2 \approx 0.2\ell_1$, and therefore ℓ_2 is much smaller than the equilibrium distance ℓ_2^0. This implies that the elastic interaction between two neighboring precipitates is most of the time repulsive. As observed in Figure 8, this repulsive force, given by the slope of the interaction energy curve, increases as $\Delta C'$ increases. This trend is consistent with the lower number of observed coagulations.

Finally, considering a configuration of two precipitates initially aligned along one cubic direction, we have performed a similar energetic analysis by varying the precipitate positions perpendicularly to this cubic direction: the less aligned the precipitates are along the initial direction, the higher the elastic energy is. It has been found that this trend is slightly more pronounced when $\Delta C'$ is small, in agreement with a stronger alignment of precipitates along the cubic directions [21].

With the above simple configurations, we have shown that the elastic energy inside the γ channels

is related to the elastic coefficient C', and that a lower inhomogeneity $\Delta C'$ leads to a weaker elastic repulsions along the cubic directions, and stronger alignments. These results shed light on the sensitivity of the coarsening mechanisms to the value of $\Delta C'$. This analysis based on prescribed precipitate shapes is relevant because the equilibrium shapes of isolated precipitates obtained with $\Delta C' = 0\%$ and $\Delta C' = 50\%$ are almost identical [21]. Note however that the equilibrium shape is slightly rounder when $\Delta C' = 50\%$ and that this shape change may participate slightly to the difference in the coagulation process. More generally, it is important to keep in mind that the above analysis is only qualitative. Indeed, in a developed microstructure, each precipitate interacts with many other precipitates and elastic interactions are known to be sensitive to the shape of the precipitates which in turn may evolve due to these interactions [29].

4. 3D analysis of the influence of $\Delta C'$

As demonstrated above, a strong inhomogeneity on the shear elastic modulus C' is required to generate 2D cuboidal microstructures composed only of square-shaped precipitates. The present section is devoted to the study of 3D microstructures to allow a direct comparison with experimental observations (§5).

First, the main differences between 2D to 3D calculations are worth being pointed out:

- For a given volume fraction τ of γ', the ratio between the channel width and the precipitate size is smaller in 3D. Indeed, in a model microstructure made of a periodic arrangement of cuboidal γ' precipitates of size ℓ_1, $\ell_2 = \ell_1(\tau^{-\frac{1}{D}} - 1)$ where ℓ_2 is the channel width and D the space dimension.

- The number of neighboring precipitates is higher in 3D, which implies that the probability for a precipitate to have at least one in-phase neighboring precipitate is also higher.

- The 2D calculations were performed within a 3D framework, by assuming that all fields are invariant along the out-of-plane [001] direction. Thus, the elastically driven morphological transition observed during the precipitate growth is from cylinder to square-based cylinder. Indeed, this differs from the sphere to cube transition in 3D as shown in [18] where it has been shown that the characteristic size of the transition in 3D is 8 times larger than the one in 2D.

These differences are expected to impact quantitatively the coarsening mechanisms. From a numerical point of view, decreasing the channel width requires a smaller discretization length, and therefore contributes to increase the CPU load of 3D computations.

3D calculations with different $\Delta C'$ values (0, 17 and 50%) have been realized in stress-free conditions starting from an initial γ disordered state. The system size is $6.8 \times 6.8 \times 6.8$ μm^3 discretized with 512^3 nodes ($d = 13.4$ nm). The discretization $d = 13.4$ nm could not be reduced further due to available computational resources. The sensitivity of the results to the discretization length is discussed at the end of the section. The microstructures obtained after 2.0 h at 950°C are shown in Figure 9. As in 2D simulations, increasing $\Delta C'$ from 0 to 50% influences the evolutions significantly: a strong inhomogeneity on C' favors cuboidal γ' precipitates whereas elongated or irregular ones are generated in the absence of inhomogeneity. The trends can be drawn from the analysis of 2D sections (Figure 10). Neighboring precipitates tend to get closer to each other when $\Delta C' = 0$, such that a large number of in-phase precipitates coagulate to form elongated and irregular-shaped γ' domains. In contrast, the microstructure obtained with $\Delta C' = 50\%$ contains many in-phase neighboring precipitates. Finally, as expected, the features of the microstructure with $\Delta C' = 17\%$ are in between those of the two other cases.

2D aspect ratios averaged over many 2D sections $\langle \ell_{min}/\ell_{max} \rangle$ are plotted in Figure 11 to quantify the trends drawn above. They are obtained by analyzing 2D sections every tenth of the 3D boxes. To improve the statistics, the measurements have been performed perpendicularly to the three cubic directions. The three calculations deliver very different results after about 1 h. Indeed, the average aspect ratio decreases continuously for $\Delta C' = 0$ while, for $\Delta C' = 17\%$ and 50%, $\langle \ell_{min}/\ell_{max} \rangle$ first decreases before reaching an almost stable value around 0.66 and 0.69, respectively.

To analyze the sensitivity of the results to space discretization, we have performed similar calculations with a grid spacing twice the previous value [21]. The qualitative differences between the microstructure evolutions with $\Delta C' = 0$, 17 and 50% remain the same. From a quantitative point of view, a slight decrease of the average aspect ratio is measured (below 0.02), which indicates the occurrence of few spurious coagulation events when the larger grid spacing is used.

Finally, a 3D energetic analysis of the elastic interactions between cubic neighboring precipitates provides the same qualitative arguments as in 2D (Fig. 8) to understand the role of $\Delta C'$ on coarsening: again, an increase in $\Delta C'$ promotes repulsive elastic interactions and gives rise to less pronounced alignments.

5. Experimental data

We have clearly shown that the microstructure evolution of Ni-based superalloys with high volume fraction of γ' is very sensitive to the inhomogeneity coefficient $\Delta C'$. In commercial superalloys, this quantity is however difficult to obtain with a good accuracy. The first reason is that the C' coefficients are very small in these alloys: values as low as 25-30GPa are usually reported above 1000K [33, 34, 35]. The second reason is related to the difficulty to synthesize multicomponent γ' bulk samples with the equilibrium compositions at the temperature of interest. Hence, although the local measurement using nano-indentation has been attempted [36, 37], the usual approach to obtain the elastic constants of the γ and γ' phases is to perform macroscopic measurements on samples made of full γ and γ+γ'. Then, a reverse engineering approach relying on mixing rules or elastic calculations on simplified configurations is used to deduce the elastic constants of the γ' phase. It is clear that the accuracy of this approach for measuring $\Delta C'$ remains an open issue.

This is why we analyze the microstructure in the AM1 commercial superalloy, before critically discussing the accuracy of the elastic constant measurements of the literature. For that purpose, we have gathered a large number of SEM images of this superalloy (e.g. Figure 1) obtained during experimental studies carried out at Onera [38, 39, 40]. After an homogenization and dissolution aging at 1300°C, all samples have experienced an isothermal holding at 1100°C during which the γ' phase appears and forms cuboidal precipitates. Finally, a final aging at 870°C is performed during which a slight increase of the precipitate volume fraction is observed. This last step reduces slightly the channel width and therefore improves the mechanical properties of the alloy, but has no significant impact on the aspect ratio of the precipitates. Therefore, the precipitate morphology in the AM1 superalloy ensues from the elastic properties of the alloy at 1100°C. We have considered images with magnifications sufficiently large to resolve accurately the matrix channels. The $2D$ average aspect ratios $\langle \ell_{min}/\ell_{max} \rangle$, as well as the surface fractions $\tau_{\gamma'}$ of γ' precipitates are reported in Table 2 with the corresponding number N_p of analyzed precipitates. The average aspect ratio is close to 0.76, indicating that most of the precipitates feature square-like morphologies. It can be noted that even with different $\tau_{\gamma'}$, there is only tiny variations of the 2D average aspect ratio.

Based on these measurements, the analysis of the phase field calculations can be used to estimate the proper value of $\Delta C'$. In 2D (Fig. 3), the average aspect ratio equals 0.76 for $\Delta C' \approx 40\%$. The 3D calculations also suggest that $\Delta C'$ is 50%, but this value may be overestimated due to some remaining spurious coagulations, as discussed above.

The elastic constants of the γ and γ' phases in AM1 have been obtained at 950°C and 1050°C in [11] using reverse engineering as proposed in [41, 42]. At 1050°C, the estimation of the elastic constants (GPa) of the coexisting phases are $C_{11}^{\gamma} = 185.1$, $C_{12}^{\gamma} = 134.0$, $C_{44}^{\gamma} = 84.2$. $C_{11}^{\gamma'} = 185.6$, $C_{12}^{\gamma'} = 129.4$, $C_{44}^{\gamma'} = 90.6$. This gives $\Delta C' = 10\%$, which is clearly a too low value to explain the measured aspect ratio in AM1. Hence, the present work strongly suggests that the usual procedure used to measure the elastic constants of the γ and γ' phases of a Ni-based superalloys may not be accurate enough to estimate the value of $\Delta C'$.

6. Conclusion

We have investigated the microstructure evolution of a binary Ni-based superalloy containing a high volume fraction of γ' precipitates. Using 2D and 3D phase field calculations, we have shown that the average aspect ratio of the cuboidal precipitates is very sensitive to the inhomogeneity $\Delta C'$ of the C' elastic constant. When $\Delta C'$ is close to zero, the microstructure contains many elongated precipitates whereas only cuboidal precipitates are obtained when $\Delta C'$ is large enough. These morphological differences result from the sensitivity of the coarsening mechanisms to $\Delta C'$: when in-phase neighboring precipitates grow, a low (resp. high) inhomogeneity promotes (resp. inhibits) coagulation. This behavior has been related to a stronger elastic repulsive interaction between precipitates when $\Delta C'$ is high.

Finally, the microstructures observed in the AM1 superalloy has been analyzed in light of the calculations. The measurement of the average aspect ratio of the γ' precipitates on 2D sections parallel to the cubic planes leads to high values between 0.75 and 0.78 corresponding to precipitates with cube-like morphology. The elastic constants reported in the literature for the γ and γ' phases in AM1 at 1050°C correspond to a low $\Delta C'$ which is not consistent with the high value of the average precipitate aspect ratio observed in this alloy. This observation suggests that, because of the low value of C' in Ni-based superalloys, the reverse engineering of the elastic constants of both γ and γ' is not accurate enough to provide $\Delta C'$. Hence, this study indicates that a closer attention must be paid to the measurement of the C' elastic constant of the γ and γ' phases when one is interested in predicting the microstructure evolution of Ni-based superalloys.

To extend the present work, it would be worth investigating the microstructure evolution when the volume fraction is reduced. Indeed, based on [43], it is expected that reducing the volume fraction induces qualitative changes towards 3D microstructures featuring 2D (plates) or 1D (line)

alignments of precipitates. In such cases, the consequences of elastic inhomogeneity may be more complex [2].

Acknowledgements

The authors acknowledge the financial support of the French Agence Nationale de la Recherche (ANR) under reference ANR-BLAN08-1-321567 (project Couphin). The authors also thank Dr. P. Caron for fruitful discussions and for providing many SEM and TEM images of superalloys.

ANNEX 1: Elastic moduli permutation

To provide additional support for demonstrating the role of $\Delta C'$ on the shape evolution of γ' precipitates, the following 2D calculations have been carried out. Starting from a disordered phase, the microstructure evolution is first computed using a given elastic inhomogeneity. Once the microstructure displays cuboidal γ' precipitates, $\Delta C'$ is set to a new value and the subsequent evolution is computed. Then, the importance of $\Delta C'$ on the precipitate shape is analyzed by inspecting the time evolution of their average aspect ratio.

This approach is illustrated in Fig. 12 with two calculations. For the first one (open squares $\square$), $\Delta C'$ is initially set to 0 until $t = 1.65$ h and subsequently changed to 50%. In the second one (full circles $\bullet$), $\Delta C'$ is set to 50% until $t = 1.65$ h and then changed to 0. The time $t = 1.65$ h corresponds to well-defined cuboidal precipitates separated by channels wide enough compared to the grid spacing $d = 6$ nm. As shown in Fig. 12, the change of $\Delta C'$ has a deep impact on the evolution of the precipitates shape. Indeed, in the first case, $\langle \ell_{min}/\ell_{max} \rangle$ first decreases from 0.78 to 0.76 when $\Delta C' = 0$ but increases from 0.76 to 0.8 when $\Delta C' = 50\%$. The opposite behavior is observed when $\Delta C'$ goes from 50% to 0 (case 2). The characteristic time of this morphological transition, estimated where the curves cross each other in Fig. 12, is about 1.5 h and corresponds to an increase of the average precipitate size of about 50%. Thus, changing $\Delta C'$ impacts the average aspect ratio significantly only after a sufficient duration for the microstructure to coarsen. This is consistent with the control of the coarsening mechanisms by the magnitude of $\Delta C'$.

Even if this sudden change of elastic constants can appear somewhat artificial, these calculations clearly illustrate that, when the microstructure evolution results from a multiple step process, the final average aspect ratio is mainly due to the elastic inhomogeneity pertaining to the last step,

provided that during this final step the microstructure has significantly coarsened. This point is of prime importance for understanding commercial superalloys for which the standard heat treatment contains several successive annealing temperatures.

	$C_{11}^{\gamma'}$	$C_{12}^{\gamma'}$	$C_{44}^{\gamma'}$	$\Delta C'$	ΔA	ΔC_{11}
a	193	140	88	0	-0.02	-0.02
b	193	140	70	0	-0.22	-0.02
c	193	140	117	0	0.29	-0.02
d	148	95	88	0	-0.02	-0.25
e	246	193	88	0	-0.02	0.25
f	193	113	132	0.51	-0.02	-0.02
g	193	113	106	0.51	-0.22	-0.02
h	193	113	177	0.51	0.29	-0.02
i	148	68	132	0.51	-0.02	-0.25
j	246	166	132	0.51	-0.02	0.25
k	193	131	97	0.17	-0.08	-0.02

Table 1: Elastic moduli (in GPa) of γ'. The elastic moduli of γ are taken from [11]: $C_{11}^{\gamma} = 197$, $C_{12}^{\gamma} = 144$ and $C_{44}^{\gamma} = 90$ GPa.

	τ_{2D}	N_p	$\langle \ell_{min}/\ell_{max} \rangle$
S_1	0.68	658	0.78
S_2	0.71	771	0.75
S_3	0.61	399	0.75

Table 2: Average aspect ratios of γ' precipitates (formed at 1100°C) measured in AM1. N_p is the number of analyzed precipitates and τ_{2D} their surface fraction.

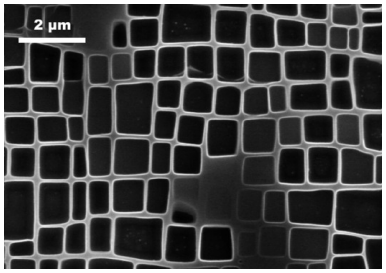

Figure 1: Scanning electron microscope observation of AM1 superalloy after a standard heat treatment [38].

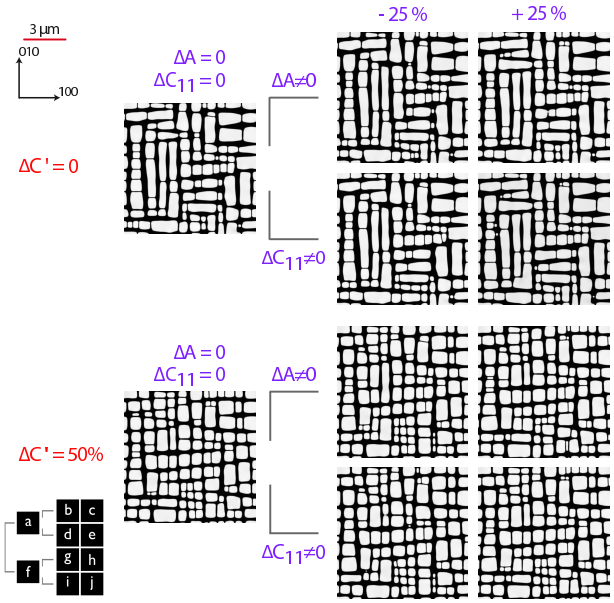

Figure 2: Concentration fields $c(\underline{\boldsymbol{r}}, t)$ of microstructures generated in stress-free conditions at $T = 950°\mathrm{C}$ during 4.8 h with the elastic moduli given in Table 1. The white and black areas correspond to the γ' and γ phases, respectively. Labels are indicated in the lower left corner.

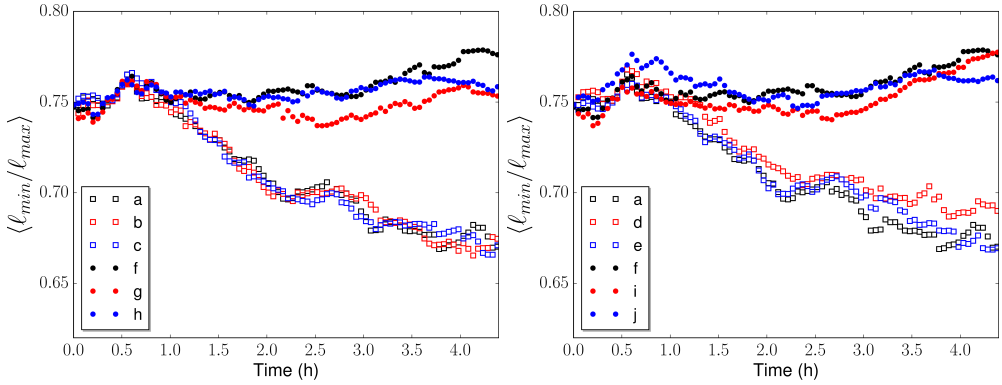

Figure 3: Time evolution of the average aspect ratio $\langle \ell_{min}/\ell_{max} \rangle$. The labels of the curves are consistent with the snapshots in Fig. 2 with $\Delta C' = 0$ and 50% represented by open squares and full circles, respectively.

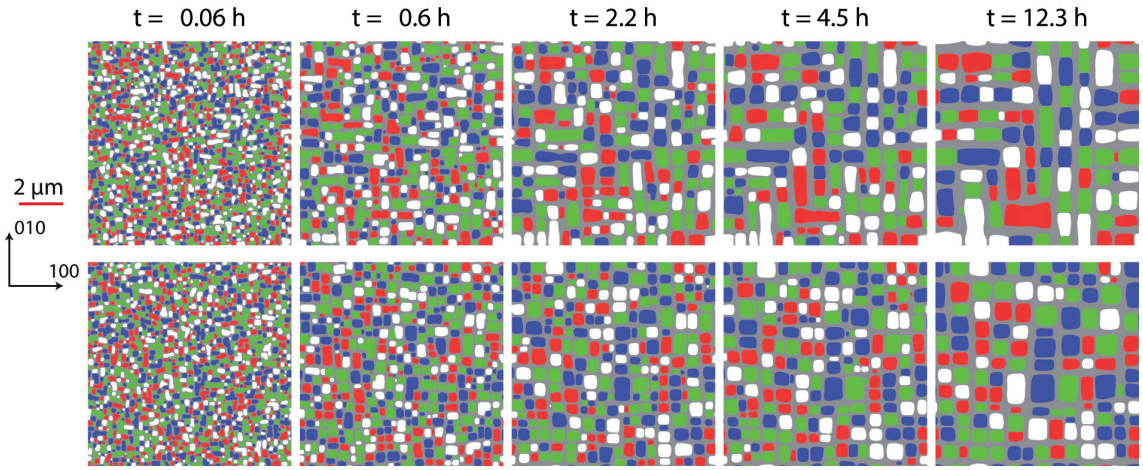

Figure 4: Microstructures generated in stress-free conditions at $T = 950°$C during 12.3 h with the elastic moduli given in Table 1, lines *a* and *f*, for $\Delta C' = 0$ (top) and $\Delta C' = 50\%$ (bottom). The grid spacing is $d = 6$ nm.

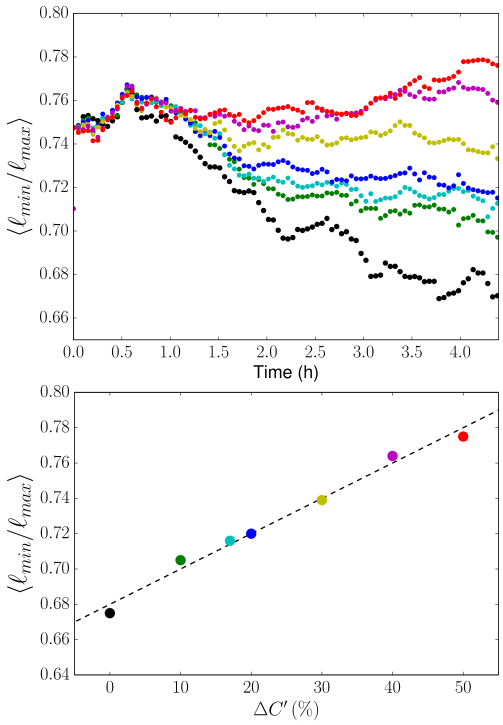

Figure 5: Aspect ratio $\langle \ell_{min}/\ell_{max} \rangle$ evolution during annealing at $T = 950°\text{C}$ for different $\Delta C'$ (top) with their corresponding values (bottom) averaged over the last 40 min. The grid size is $d = 9$ nm.

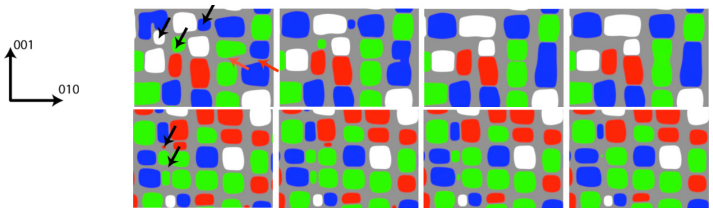

Figure 6: Snapshots illustrating the coarsening mechanisms for the evolution with $\Delta C' = 0$ (top) and 50% (bottom): Ostwald ripening - black arrows ; coagulation - red arrows ($d = 6$ nm).

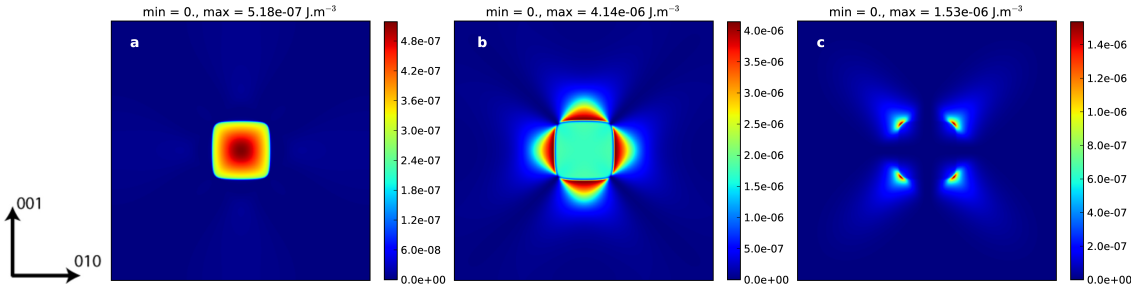

Figure 7: Contributions to the elastic energy density related to the three elastic moduli: (a) B, (b) C' and (c) C_{44}, for a single γ' precipitate. The system size is 4.6×4.6 μm^2 box. Elastic constants are from line *f* in Table 1.

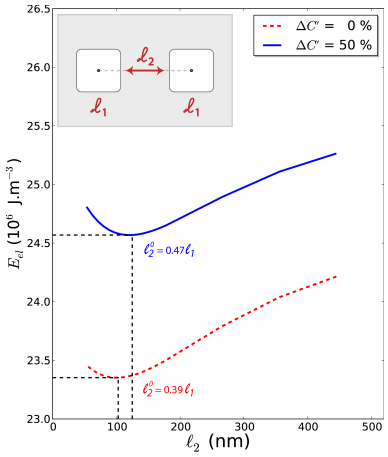

Figure 8: Elastic energy as a function of the separating distance ℓ_2 between two cuboidal precipitates in a 4.6×4.6 μm^2 box.

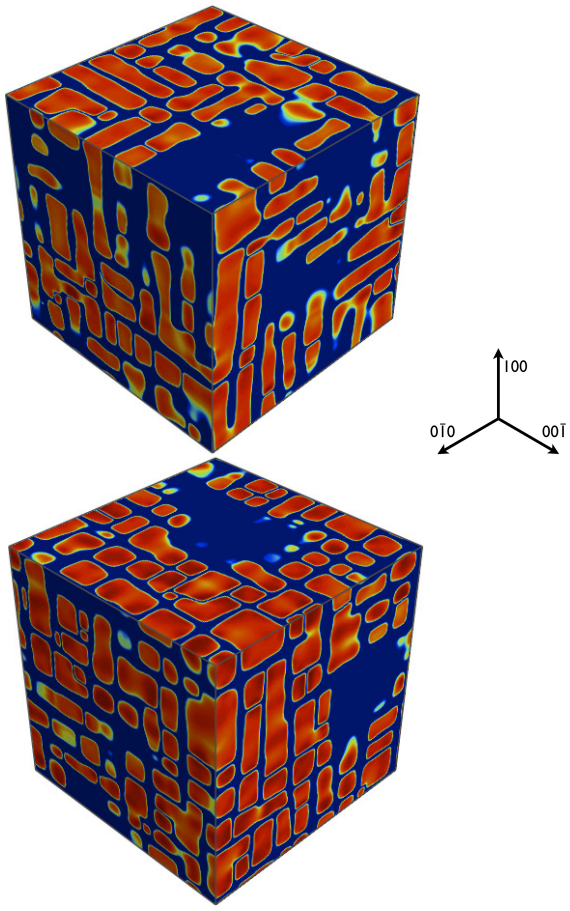

Figure 9: Concentration maps obtained in stress-free conditions after 2 h at $T = 950°$C: line *a* in Table 1 and $\Delta C' = 0$ (top) ; line *f* in Table 1 and $\Delta C' = 50\%$ (bottom). The color scale is dark blue-yellow-red (values going from 0.15 to 0.25).

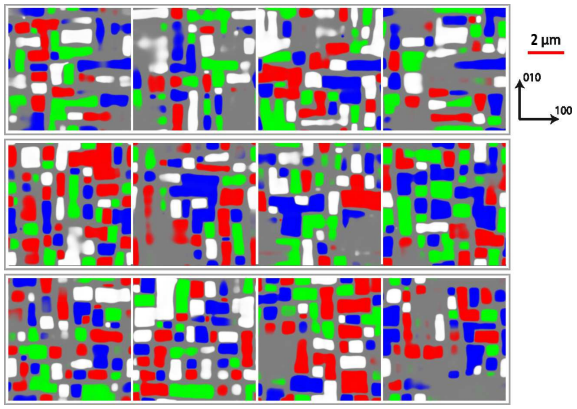

Figure 10: From left to right: sections perpendicular to [001] every $153d$ of the 3D box at $t = 2$ h.
Top row: $\Delta C' = 0$ and row a in Table 1.
Middle row: $\Delta C' = 17\%$ and row k in Table 1. Bottom row: $\Delta C' = 50\%$ and row f in Table 1.

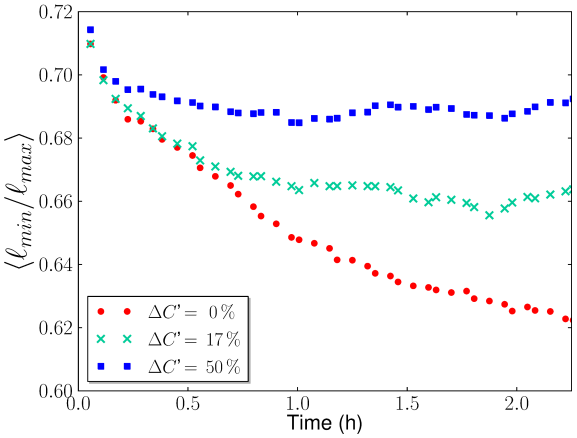

Figure 11: Evolution, for different $\Delta C'$, of the average aspect ratio $\langle \ell_{min}/\ell_{max} \rangle$ measured on 2D sections perpendicular to the cubic directions of the $3D$ box.

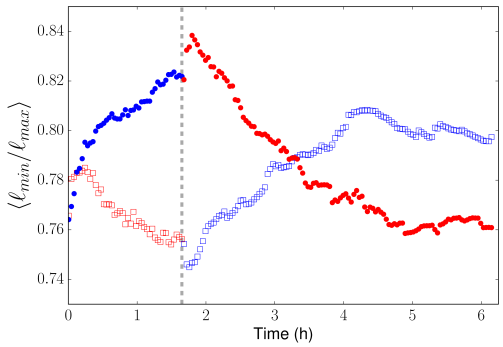

Figure 12: Evolution of the average aspect ratio for cases where $\Delta C'$ is changed at $t = 1.65$ h (dashed line). The red (resp. blue) parts corresponds to $\Delta C' = 0$ (resp. 50%) and elastic constants at line *a* (resp. *f*) in 1. The grid spacing is $d = 6$ nm.

References

[1] T. Khan, P. Caron, in: J. Bilde-Sorensen, N. Hansen, A. Horsewell, T. Leffers, H. Lilholt (Eds.), Deformation of Multi-Phase and Particle Containing Materials, Riso National Laboratory, 1983, pp. 333–338.

[2] A. J. Ardell, Phil. Mag. 94 (2014) 2101–2130.

[3] H. Nishimori, A. Onuki, Phys. Rev. B 42 (1990) 980–983.

[4] Y. Wang, L. Q. Chen, A. G. Khachaturyan, Acta Metall. Mater. 41 (1993) 279–296

[5] J. Z. Zhu, T. Wang, A. J. Ardell, S. H. Zhou, Z. K. Liu, L. Q. Chen, Acta Mater. 52 (2004) 2837–2845.

[6] T. Wang, G. Sheng, Z. K. Liu, L. Q. Chen, Acta Mater. 56 (2008) 5544 – 5551.

[7] G. Boussinot, A. Finel, Y. Le Bouar, Acta Mater. 57 (2009) 921–931.

[8] Y. Wang, D. Banerjee, C. C. Su, A. G. Khachaturyan, Acta Mater. 46 (1998) 2983–3001.

[9] V. Vaithyanathan, L. Q. Chen, Acta Mater. 50 (2002) 4061–4073.

[10] A. Gaubert, A. Finel, Y. Le Bouar, G. Boussinot, in: D. Jeulin, S. Forest (Eds.), Continuum Models and Discrete Systems CMDS 11, Les Presses de l'École des Mines de Paris, 2008, pp. 161–166.

[11] A. Gaubert, Y. Le Bouar, A. Finel, Phil. Mag. B 90 (2010) 375–404.

[12] N. Zhou, C. Shen, M. Mills, Y. Wang, Phil. Mag. B 90 (2010) 405–436.

[13] M. Cottura, Y. L. Bouar, A. Finel, B. Appolaire, K. Ammar, S. Forest, J. Mech. Phys. Solids 60 (2012) 1243–1256.

[14] A. Gaubert, M. Jouiad, J. Cormier, Y. Le Bouar, J. Ghighi, Acta Mater. 84 (2015) 237–255.

[15] C. Sagui, D. Orlikowski, A. M. Somoza, C. Roland, Phys. Rev. E 58 (1998) 4092–4095.

[16] A. Onuki, A. Furukawa, Phys. Rev. Lett. 86 (2001) 452–455.

[17] J. Zhu, L. Q. Chen, J. Shen, Model. Simul. Mater. Sc. 9 (2001) 499–511.

[18] G. Boussinot, Y. Le Bouar, A. Finel, Acta Mater. 58 (2010) 4170–4181.

[19] S. Y. Hu, L. Q. Chen, Acta Mater. 49 (2001) 1879–1890.

[20] Y. Tsukada, Y. Murata, T. Koyama, M. Morinaga, Mater. Trans. 50 (2009) 744–748.

[21] M. Cottura, Ph.D. thesis, Université Paris VI (2013).

[22] P. H. Leo, J. S. Lowengrub, H. J. Jou, Acta Mat. 46 (1998) 2113–2130.

[23] K. Thornton, J. Agren, P. W. Voorhees, Acta Mat. 51 (2003) 5675–5710.

[24] F. Fujiwara, M. Watanabe, Z. H. N. Nemoto, K. Noumi, T. Simozaki, in: K. O. M. Koiwa, T. Miyazaki (Eds.), International Conference on Solid-Solid Transformations, in JIMIC-3, 1999, pp. 481–484.

[25] L. Thuinet, A. De Backer, A. Legris, Acta Mater. 60 (2012) 5311–5321.

[26] A. J. Ardell, V. Ozolins, Nat. Mater. 4 (2005) 309 – 316.

[27] A. Royer, P. Bastie, M. Véron, Acta Mater. 46 (1998) 5357–5368.

[28] F. Diologent, P. Caron, T. d'Almeida, A. Jacques, P. Bastie, Nucl. Instrum. Meth. B 200 (2003) 346–351.

[29] C. H. Su, P. W. Voorhees, Acta Mater. 44 (1996) 1987–1999.

[30] W. C. Johnson, P. W. Voorhees, J. Appl. Phys. 61 (1987) 1610–1619.

[31] C. H. Su, P. W. Voorhees, Acta Mat. 44 (1996) 2001–2016.

[32] H. A. Calderon, G. Kostorz, L. Calzado-Lopez, C. Kisielowski, T. Mori, Phil. Mag. Lett. 85 (2005) 51–59.

[33] T. Miyazaki, K. Nakamura, H. Mori, J. Mater. Sci. 14 (1979) 1827–1837.

[34] T. M. Pollock, A. S. Argon, Acta Metall. et Mater. 42 (1994) 1859–1874.

[35] A. Hazotte, T. Grosdidier, S. Denis, Scripta Mater. 34 (1996) 601–608.

[36] B. Gan, H. Murakami, R. Maass, L. Meza, J. Greer, T. Ohmura, S. Tin, in: R. C. R. S. Huron (Ed.), Superalloys 2012: 12th international Symposium in Superalloys, TMS, 2012, pp. 83–91.

[37] I. Povstugar, P.-P. Choi, S. Neumeier, A. Bauer, C. H. Zenk, M. Göken, D. Raabe, Acta Mater. 78 (2014) 78–85.

[38] F. Diologent, PhD Thesis, Université Paris XI-Orsay (2002).

[39] F. Diologent, P. Caron, T. d'Almeida, A. Jacques, P. Bastie, Nucl. Instrum. Meth. B 200 (2003) 346–351.

[40] F. Diologent, P. Caron, Mater. Sci. and Eng. A 385 (2004) 245–257.

[41] M. Fahrmann, W. Hermann, E. Fahrmann, A. Boegli, T. M. Pollock, H. G. Sockel, Mater. Sci. and Eng. A 260 (1999) 212–221.

[42] D. Sieborger, H. Knake, U. Glatzel, Mater. Sci. and Eng. A 298 (2001) 26–33.

[43] A. C. Lund, P. W. Voorhees, Acta Mater. 50 (2002) 2585–2598.